



Dynamic trap of Ni at elevated temperature for yielding high-efficiency methane dry reforming catalyst

Dedong He^{a,b,c}, Shaojie Wu^a, Xiaohua Cao^{a,b,c}, Dingkai Chen^{a,b,c,*}, Lei Zhang^{b,c,e}, Yu Zhang^d, Yongming Luo^{a,b,c,d,*}

^a Faculty of Chemical Engineering, Kunming University of Science and Technology, Kunming 650500, PR China

^b The Innovation Team for Volatile Organic Compounds Pollutants Control and Resource Utilization of Yunnan Province, Kunming 650500, PR China

^c The Higher Educational Key Laboratory for Odorous Volatile Organic Compounds Pollutants Control of Yunnan Province, Kunming 650500, PR China

^d Faculty of Environmental Science and Engineering, Kunming University of Science and Technology, Kunming 650500, PR China

^e School of Environmental Science and Engineering, Yancheng Institute of Technology, Yancheng 224051, PR China

ARTICLE INFO

Keywords:

Dynamic trap
High-temperature capture
Silanol nests
Small Ni nanoparticle
Dry reforming

ABSTRACT

Highly dispersed and stable metal catalysts with small nanoparticles have received extensive attention in elevated-temperature thermocatalytic process. However, the available strategies to stabilize metal sites, by constructing defective structures on catalyst supports and developing controllable preparation steps at room temperature, show limited effect, because these active metal sites can be mobile and sintering at elevated temperature. Herein, dealuminated Beta zeolite with abundant surface defects of silanol nests is applied as support, then dynamic trap strategy and subsequent reduction process at elevated temperature is devoted to transfer Ni-based precursors into the silanol nests, thus obtaining small nanoparticles Ni catalysts that are suitable for high-temperature methane dry reforming (DRM). Some *in-situ* characterization processes and the ingenious designed experiments are performed to identify the dynamic trapping process. The rational fabricated catalysts exhibit high catalytic reactivity for DRM reaction in long-term operation.

1. Introduction

In the last decades, high dispersion of active components with small nanoparticles has attracted much attention in heterogeneous catalysis fields (especially thermocatalysis), since these highly dispersed small nanoparticle metal sites are desirable to maximize active component efficiency [1,2], which shows excellent catalytic reactivity in heterogeneous catalytic reactions, such as dry reforming of methane (DRM) [3,4], CO oxidation [5], and hydrogenation reaction *etc.* [6,7]. However, the high dispersed state, as is well-known, is difficult to be maintained because of sintering at elevated temperature over 600 °C, finally leading to the decrease in catalytic activity [8–11]. Therefore, high temperature tolerance of catalyst is key reaction-limiting step unless these mobile active species can be effectively trapped. Against the above background, researchers' much effort is to develop new strategies for strengthening the metal-support interaction in order to obtain highly dispersed catalysts with sinter-resistant for heterogeneous catalysis reactions [12–15].

Precise regulation of the support structure is an efficient path to obtain a strong metal-support interaction. Thereinto, controlled construction of defects on commonly used supports of CeO₂ and Al₂O₃ is an effective approach to hinder the agglomeration and migration of active metal species on the supports, because constructed defects can offer as “traps” to seize metal precursors and anchor active metal species [16,17]. Particularly, hydroxyl groups on the surface of typical Al₂O₃ and SiO₂ supports are generally considered as the bridge of constructing appropriate interaction between metal and support to obtain highly dispersed active components on the supports [18,19]. However, general Al₂O₃ and SiO₂ supports have inferior structures, leading to ill-defined surface-active species. For example, although abundant hydroxyl over Al₂O₃ brings strong metal-support interaction to anchor metal species, while inactive nickel aluminate phase of NiAl₂O₄ forms inevitably under elevated-temperature condition, restricting effective utilization of Ni in the commercial Al₂O₃ support [14]. Furthermore, conventional SiO₂ as a carrier can increase the exposure of active sites, but the tendency is to

* Corresponding authors at.

E-mail addresses: cdk684983@163.com (D. Chen), environcatalysis@kust.edu.cn (Y. Luo).

<https://doi.org/10.1016/j.apcatb.2024.123728>

Received 30 August 2023; Received in revised form 7 January 2024; Accepted 10 January 2024

Available online 12 January 2024

0926-3373/© 2024 Elsevier B.V. All rights reserved.

form larger particles and face sintering challenges in high temperature reactions, which is probably due to weak metal-support interaction between SiO₂ and active metal sites [20].

Recently, BEA zeolites, as a replacement for common SiO₂ support, have been widely concerned due to their high surface areas, regular pore channels and good thermal stability [21,22]. More importantly, the dealumination of BEA zeolite has been developed as an excellent strategy to further improve metal-support interaction, since they can generate abundant vacant T-sites associated with silanol nests, creating the possibility to stabilize metal precursors [23,24]. Although several attempts have been reported [10,25,26], it still remains a challenge to design feasible strategy for prompting the active metal completely into the nests to reach deserved properties of strong anti-sintering/inactivation during thermocatalysis reactions. Furthermore, the highly dispersed state of active sites obtained from traditional strategies of impregnation, deposition-precipitation and strong electrostatic adsorption are difficult to be maintained [27–32], since once the prepared sample is heated at high temperature, the mobility of the introduced metal obtained *via* the initial preparation steps at room temperature causes the formation of thermodynamically stable structure of larger particles [33]. In addition to above traditional strategies, the concept of active particles trapping, in which those mobile atoms can be *in situ* trapped, has attracted much attention in heterogeneous catalysis. For example, Datye et al. reports an atom trapping strategy to prepare CeO₂-supported Pt single-atom-site catalyst (SASCs). This method mixes 1 wt% Pt NPs/Al₂O₃ with CeO₂ and then ages the mixture in the air at 800 °C. During the aging, CeO₂ rods or polyhedra capture mobile Pt atoms from Pt NPs/Al₂O₃ and form SASCs [34]. Overall, the fundamental question is that how to control the construction of the support and effectively introduce active metal components for heightening the metal-support interaction, ultimately achieving high-dispersion and anti-sintering catalysts for elevated temperature applications.

Among thermocatalysis reactions, dry reforming of methane (DRM) is an environmentally friendly process, because DRM reaction can not only reduce greenhouse gas emissions (CH₄ and CO₂), and its product of syngas (CO/H₂) is an important intermediate in the synthesis of valuable chemical products [14,35,36]. Ni-based catalysts are usually employed for DRM reactions due to its high potential as a non-noble metal catalyst with economic benefits and excellent performance [37–39]. However, one major issue concerning Ni-based catalysts is their rapid deactivation due to metal sintering during high temperature process [40], limiting the feasibility of their large-scale industrial implementation. Therefore, developing stable small-nanoparticle nickel catalysts with strong sintering-resistance still remains challenge.

In this study, BEA zeolite is firstly dealuminated to form silanol nests within the T-vacant sites. Subsequently, nickel (II) acetylacetonate (Ni (acac)₂) is choosed as nickel-based precursors, since it can perform vapor-phase diffusion at high temperature (about 230 °C) and be decomposed to form NiO at certain temperature. The vapor-phase nickel-based precursors are diffused into the silanol nest at high temperature of 300 °C to realize dynamic capture of nickel components, finally generating highly dispersed NiO small-nanoparticles. This novel dynamic trap strategy and the subsequent reduction process at elevated temperature are devoted to transfer Ni-based precursors into the silanol nests. The diffusion of nickel precursors accompanied by dehydration condensation of hydroxyl sites from silanol nest at elevated temperature provides suitable opportunity to achieve dynamic capture of metal sites, thus obtaining small nanoparticles Ni catalysts that are suitable for high-temperature DRM. This unique strategy displays dual-role of anchoring active Ni sites and benefiting outstanding DRM performance when compared to current reported Ni-based DRM catalysts. This finding opens up new opportunities for the engineering of high-performance DRM catalysts, and provides applicability for the synthesis of high-efficiency heterogeneous catalyst within small nanoparticles.

2. Experimental

2.1. Catalyst preparation

2.1.1. Synthesis of dealuminated Beta zeolite

Commercial HAlBeta with a Si/Al ratio of 25 was purchased from Yangzhou Zhonghe Petrochemical Research Institute Co., Ltd., and treated with aqueous nitric acid solution (13 mol/L) at 80 °C for 12 h under continuous stirring. Then, the samples were extracted, washed with deionized water and dried at 80 °C for 12 h to remove all Al ions. The obtained products were recorded as SiBeta. Meanwhile, 1 g of SiBeta was calcined at 500 °C for 6 h to obtain SiBeta-C.

2.1.2. Synthesis of Ni-based catalysts

For Ni/SiBeta, a theoretical Ni loading of 2.5 wt% was obtained by adding the appropriate SiBeta zeolite and nickel acetylacetonate (Ni (acac)₂) into an agate mortar, and grinding continuously for 30 min. Then, the obtained powder was calcined at 300 °C for 6 h at a heating rate of 10 °C/min in air. ICP-OES result shows that the actual Ni loading is 2.4 wt%, close to the theoretical Ni loading of 2.5 wt%. Similarly, Ni/SiBeta-C and Ni/HAlBeta catalysts were prepared using SiBeta-C and HAlBeta as supports.

For comparison, three common Ni based catalysts of Ni/Al₂O₃, Ni/SiO₂ and Ni/SiBeta-I were synthesized by initial wet impregnation (IWI) method. An appropriate amount of Ni (NO₃)₂·6 H₂O solution was respectively added to γ-Al₂O₃, amorphous SiO₂ and SiBeta (γ-Al₂O₃ and amorphous SiO₂ were provided by Aladdin), and stirred continuously for 2 h, the theoretical Ni loading was 2.5 wt%. The obtained slurry was then dried at 80 °C overnight, and calcined at 500 °C for 6 h at a heating rate of 10 °C/min under air atmosphere. Besides, two designed catalysts of Ni/SiBeta-mixed and Ni/SiBeta-separated were given in the [Supporting Information \(SI\)](#).

2.2. Catalyst characterization

Characterization of catalysts, including inductively coupled plasma optical emission spectrometer (ICP-OES), *in-situ* X-ray diffraction (*in-situ* XRD), hydrogen temperature program reduction (H₂-TPR), H₂-chemisorption, quasi-*in situ* X-ray photoelectron spectroscopy (quasi-*in situ* XPS), transmission electron microscopy (TEM), Fourier transform infrared (FT-IR), pyridine as probe molecule of FT-IR (Py-FTIR), *in situ* Fourier transform infrared (*in-situ* FT-IR), CO₂-CH₄-dosing *in situ* diffuse reflectance infrared Fourier transform spectroscopy (DRIFTS), thermogravimetric analysis (TGA), low-temperature electron paramagnetic resonance (LT-EPR), UV–vis diffuse reflectance spectroscopy (UV–vis-DRS), ¹H-solid state nuclear magnetic resonance (¹H NMR), X-ray absorption spectroscopy (XAS), and temperature-programmed desorption of CO₂ (CO₂-TPD) were recorded in the SI.

2.3. Catalytic reactivity measurements

Catalytic measurements of DRM reaction were performed in a fixed-bed quartz reactor with 5 mm I.D. at atmospheric pressure. 60 mg of catalyst (40–60 mesh) was loaded into the middle of the reaction tube, and then reduced by a flow rate of 10 vol% H₂/Ar (30 mL/min) for 1 h at 750 °C, followed by N₂ bubbling for 1 h to remove the remaining gas. Next, gas fractions (CH₄/CO₂/N₂ = 1/1/1) at overall flow velocity of 100 mL/min were detected by an online gas chromatograph (GC, Fuli 9790II) equipped with two TCD and one FID detectors. The conversions of CH₄ or CO₂ as well as H₂/CO were calculated using the formula:

$$X_{CH_4}(\%) = \frac{[CH_4]_{in} - [CH_4]_{out}}{[CH_4]_{in}} * 100$$

$$X_{CO_2}(\%) = \frac{[CO_2]_{in} - [CO_2]_{out}}{[CO_2]_{in}} * 100$$

$$H_2/CO = \frac{[H_2]_{out}}{[CO]_{out}}$$

3. Results and discussion

3.1. Creation of silanol nests in Beta zeolites and dynamic trap of Ni

It is well known that after treatment with concentrated nitric acid, the framework aluminum located at the T sites in Beta zeolite can be removed [31], and a large number of hydrogen-bonded silanol groups, also known as silanol nests, are formed in T-vacant sites. In order to explore the changes in the silanol nest structure of T-vacant sites within Beta zeolites after different treatments, a series of characterizations, including ^1H MAS NMR, FT-IR, LT-EPR and XRD, are performed in Fig. 1.

The ^1H MAS NMR is considered as a useful technique to confirm complete removal of Al framework upon dealumination and formation of silanol nests. In the ^1H MAS NMR spectrum, the peaks at 4.52 ppm and 4.41 ppm are assigned to hydrogen bonding interactions in the silanol nests, and the peaks at 1.29 ppm and 5.85 ppm are ascribed to the surface Al-OH groups and H-linked Si-OH in zeolites, respectively, and the peaks at 2.63 ppm and 2.91 ppm corresponds to the presence of

internal Si-OH groups [24,41]. SiBeta support (Fig. 1a) is obtained by dealumination of HAlBeta (Fig. 1c), and the signal of Al-OH group decreases sharply, accompanying by the increase of silanol nest signal, which indicates the Al in the zeolite framework is almost removed after nitric acid treatment, and a large amount of silanol nest is formed in the T-vacant sites. SiBeta-C (Fig. 1b) shows that the silanol nests and other hydroxyl signals decrease after calcination.

The variation of the silanol groups closely linked to the T-vacant sites in the dealuminated zeolite are further analyzed by infrared spectroscopy. As shown in Fig. S1a, HAlBeta has no obvious band between 900–1000 cm^{-1} , while SiBeta has a band located at 956 cm^{-1} , attributed to the silanol nests produced by the dealumination of HAlBeta [42]. In SiBeta-C, the characteristic band at 956 cm^{-1} reduces significantly, which is consistent with the results of ^1H MAS NMR. Furthermore, the relative hydroxyl intensity of the catalysts before and after dealumination is compared by the difference of bands at 1630 cm^{-1} and 3467 cm^{-1} (Fig. S1b, c), respectively assigned to the bending vibration of the hydroxyl group and the surface Si-OH [43,44]. The higher band intensity of SiBeta and SiBeta-C samples suggests that the concentration of hydroxyl group increases after dealumination treatment.

Furthermore, Fig. S2a shows small angle XRD pattern of SiBeta and HAlBeta. There are characteristic peaks of Beta zeolite occurring for both samples, suggesting that the dealumination treatment does not

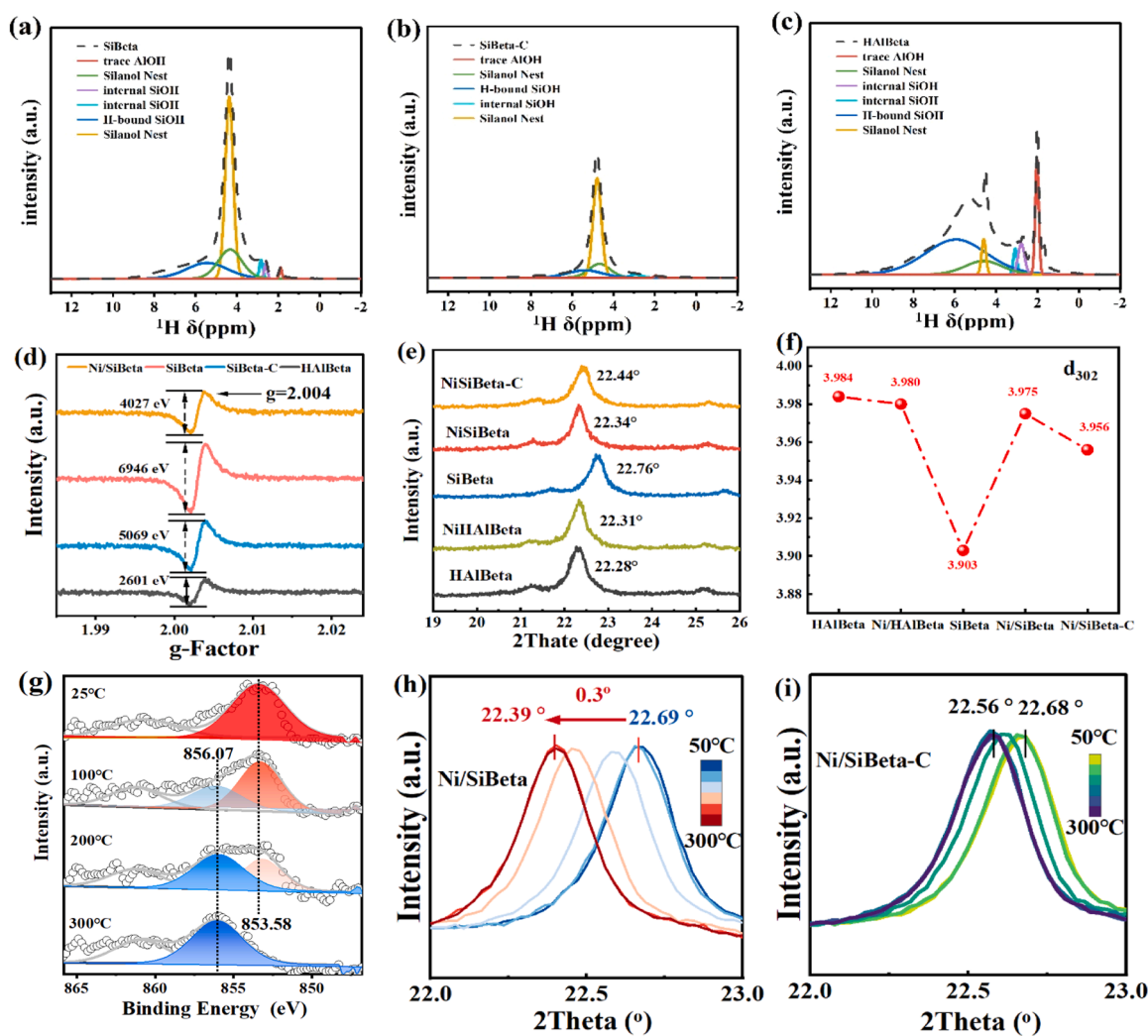


Fig. 1. Characterizations of silanol nest formation and Ni trapping by silanol nests on Beta zeolite during heating in air flow atmosphere: (a-c) ^1H NMR, (d) LT-EPR, (e) XRD, (f) d_{302} spacing value of BEA zeolite, (g) quasi *in situ* X-ray photoelectron spectroscopy (XPS) of uncalcined Ni/SiBeta, and *in situ* XRD of (h) uncalcined Ni/SiBeta and (i) uncalcined Ni/SiBeta-C.

cause structural changes in Beta zeolite. Besides, the N_2 adsorption/desorption isotherms of SiBeta and HAlBeta zeolites in Fig. S2b have no significant difference, both displaying the characteristics of type IV isotherms. These results prove that the crystal and skeleton structure of Beta zeolite have no significant damage after dealumination treatment. For comparison purposes, Table S1 summarizes the structural properties of both samples, including BET specific surface area as well as pore size and volume information. The similar structural properties of SiBeta and HAlBeta again verify that the dealumination process regulated by aqueous nitric acid solution does not damage the structure of the support. In addition, the high surface area and abundant pore structure of Beta zeolite provide the conditions for the high dispersion of active Ni species.

The observed signal for the free electron value $g = 2.0004$ in the low-temperature EPR measurements, as shown in Fig. 1d, is assigned to defects structure in the catalysts [17]. The defects of the catalysts after different treatments are compared by the difference in the vertical axis signal. The defect signals of SiBeta, SiBeta-C and HAlBeta zeolite are 6946 eV, 5069 eV and 2601 eV, respectively. SiBeta zeolite shows the strongest defect signal, which means that the removal of framework Al results in a large number of defect sites. Notably, it can be seen that the signal of Ni/SiBeta catalyst drops to 4027 eV after Ni introduction, indicating that the introduced Ni species, mainly anchored within silanol nests, occupy T-vacant sites.

The shift of X-ray diffraction pattern in $d_{(302)}$ plane of BEA zeolite and calculated unit cell parameters are shown in Fig. 1e, f, to further confirm Ni is trapped by silanol nests. After introducing Ni into HAlBeta, the offset of $d_{(302)}$ is small, and unit cell parameters have no significant changes, concluding that Ni species only stay on the surface of the zeolite and have no obvious effect on the BEA lattice, due to the lack of T-vacant sites. However, the $d_{(302)}$ diffraction peak of SiBeta zeolite after dealumination shifts to 22.76° and the lattice spacing also decreases to 3.903, indicating that the BEA lattice shrinks after the removal of framework Al. Surprisingly, the crystal phase $d_{(302)}$ of Ni/SiBeta shifts back to 22.34° compared with that of SiBeta, which is related to the BEA lattice expansion (lattice spacing increases from 3.903 to 3.975) caused by Ni occupying T-vacant sites of BEA, confirming capture of nickel by silanol nests. It is noticed that the $d_{(302)}$ of Ni/SiBeta-C only shifts back to 22.44° , namely, the BEA lattice expansion (lattice spacing increases to 3.956) is less obvious, indicating that less T-vacant sites in SiBeta after calcination allow less Ni occupy the T-vacant sites, further implying the capture of nickel is closely related to the silanol nests.

In order to gain an in-depth understanding of capture process of Ni by silanol nests, a series of *in-situ* experiments are conducted, including *in-situ* FTIR, quasi *in situ* X-ray photoelectron spectroscopy, UV-vis spectroscopy, and *in-situ* X-ray diffraction. *In situ* FT-IR is used to study the change process of acetylacetonate nickel as a precursor over nickel-based catalysts during high temperature calcination, as shown in Fig. S3a. The bands at 1728 and 1703 cm^{-1} are assigned to pure ketone carbonyl, corresponding to C=O asymmetric and symmetric stretching mode vibrations, respectively. Besides, the broad band at $1550\text{--}1650\text{ cm}^{-1}$ is caused by C=C vibration [45]. All peaks have the strong signal at 50°C , and the peak signals gradually decrease with the increase of temperature until they disappear completely at 300°C , indicating that the nickel acetylacetonate gradually decompose during heating treatment. The TGA curves of Fig. S4 under air and N_2 also show that the nickel acetylacetonate almost decomposes at 300°C . Meanwhile, the band between $900\text{--}1000\text{ cm}^{-1}$ (Fig. S3b), assigned to silanol nest signal, gradually decreases with increasing temperature, implying Ni species gradually occupy T-vacant sites accompanying by the decomposition of nickel acetylacetonate, providing first direct evidence to confirm the capture of Ni by silanol nests.

Quasi *in situ* X-ray photoelectron spectroscopy is illustrated in Fig. 1g to further study the change process of Ni species in the $2p_{3/2}$ orbital of Ni/SiBeta catalyst during calcination. Two peaks appear at 853.58 eV and 856.07 eV are attributed to NiO state [46], and it is believed that

electron transfer from NiO to support leads to the peaks shift to higher energy values. In this figure, the low binding energy peak is attributed to nickel oxide species in weak binding with the support, caused by the nickel acetylacetonate on the surface of support. The high binding energy peak can be attributed to strong binding between NiO small-nanoparticles and T-vacant sites, due to occurring electron transfer from NiO to the T-vacant sites. At room temperature, the main binding energy peak, assigned to low metal-support interactions of Ni^{2+} (nickel acetylacetonate)-Zeolite, exists at 853.58 eV. As the temperature increases, low binding energy peak gradually becomes smaller and the high binding energy peak strengthens, until it completely transforms into a single high binding energy peak at 856.07 eV at 300°C . The result indicates that more and more nickel oxide species occur charge transfer in case of Ni captured by T-vacant sites during heating process, providing second direct proof to prove that the nickel acetylacetonate species are gradually trapped by T-vacant sites in nickel oxide state. Besides, the changes of Ni coordination environment are also investigated by UV-vis spectroscopy, and the results are shown in Fig. S3c. Signals in the range of 270 nm and 388 nm for all samples are connected with ligand metal charges from 2p orbital transfer of O^{2-} to 3d orbital of Ni^{2+} [47]. With the increase of temperature, the peak at this position changes from a sharp peak to a broad peak, belonged to the $O^{2-}(2p) \rightarrow Ni^{2+}(3d)$ charge transfer of octahedral Ni^{2+} in NiO small-nanoparticles [3], revealing the decomposition process of acetylacetonate into small NiO nanoparticles during the heating stage, responding to above quasi *in situ* XPS results.

In-situ XRD pattern (Fig. 1h, i) shows the shift of diffraction peaks of $d_{(302)}$ crystal surface at different temperatures ($50\text{--}300^\circ\text{C}$), which provides third direct evidence to confirm the process that Ni is gradually trapped by T-vacant sites. It is firstly noticed that $d_{(302)}$ diffraction peaks of uncalcined Ni/SiBeta catalyst (Fig. 1h) at 50°C is located at $2\theta = 22.69^\circ$, close to the 2θ (22.76°) of SiBeta in Fig. 1e, indicating that nickel acetylacetonate only stays on the surface of the zeolite support, and lattice of zeolite is therefore not affected. With the increase of calcination temperature, the diffraction peak continuously shifts to a lower position until 22.39° at 300°C due to the expansion of the zeolite crystal phase, resulted from Ni occupying T-vacant sites of BEA zeolite, thus providing the process that Ni is gradually trapped by silanol nests. Fig. 1i shows that Ni/SiBeta-C catalyst has a smaller shift of peak position compared to Ni/SiBeta catalyst with the increase of temperature, which means that lattice expansion of treated zeolite with less silanol nests is not obvious, implying that less Ni species occupy the T-vacant sites. The results further prove that there is a direct correlation between capture of nickel and the existence of silanol nests.

3.2. Designed experiments for certifying the dynamic trap process

Above sections have provided several direct proofs to verify that Ni is trapped by silanol nest. To answer the remained question that how they are formed, a series of additional experiments are designed. Nickel acetylacetonate and SiBeta support are loaded into a tubular reactor in two different forms: (i) a physical mixture of nickel acetylacetonate and SiBeta, called Ni/SiBeta-mixed (Fig. 2a); (ii) nickel acetylacetonate and SiBeta in the form of two layers separated by a quartz wool, named Ni/SiBeta-separated (Fig. 2d). After calcination, both catalysts yield a transformation to a uniform brown color, indicating that NiO is uniformly distributed on the SiBeta zeolite. As Ni is present in SiBeta zeolite, there must be a gas-phase transport of Ni-containing species to the SiBeta supports, since nickel acetylacetonate and support layers are separated by the quartz wool. Besides, statistics of Ni particle size over the reduced Ni/SiBeta-mixed (Fig. 2b) and Ni/SiBeta-separated (Fig. 2e) are performed on TEM and STEM. Above results indicate that Ni is trapped by SiBeta supports with abundant silanol nests via vapor-phase-trapping process. Although both catalysts exist the difference in the performance due to different actual Ni content of Ni/SiBeta-Mixed (2.16%) and Ni/SiBeta-Separated (1.45%), Fig. 2c, f and Fig. S5 show

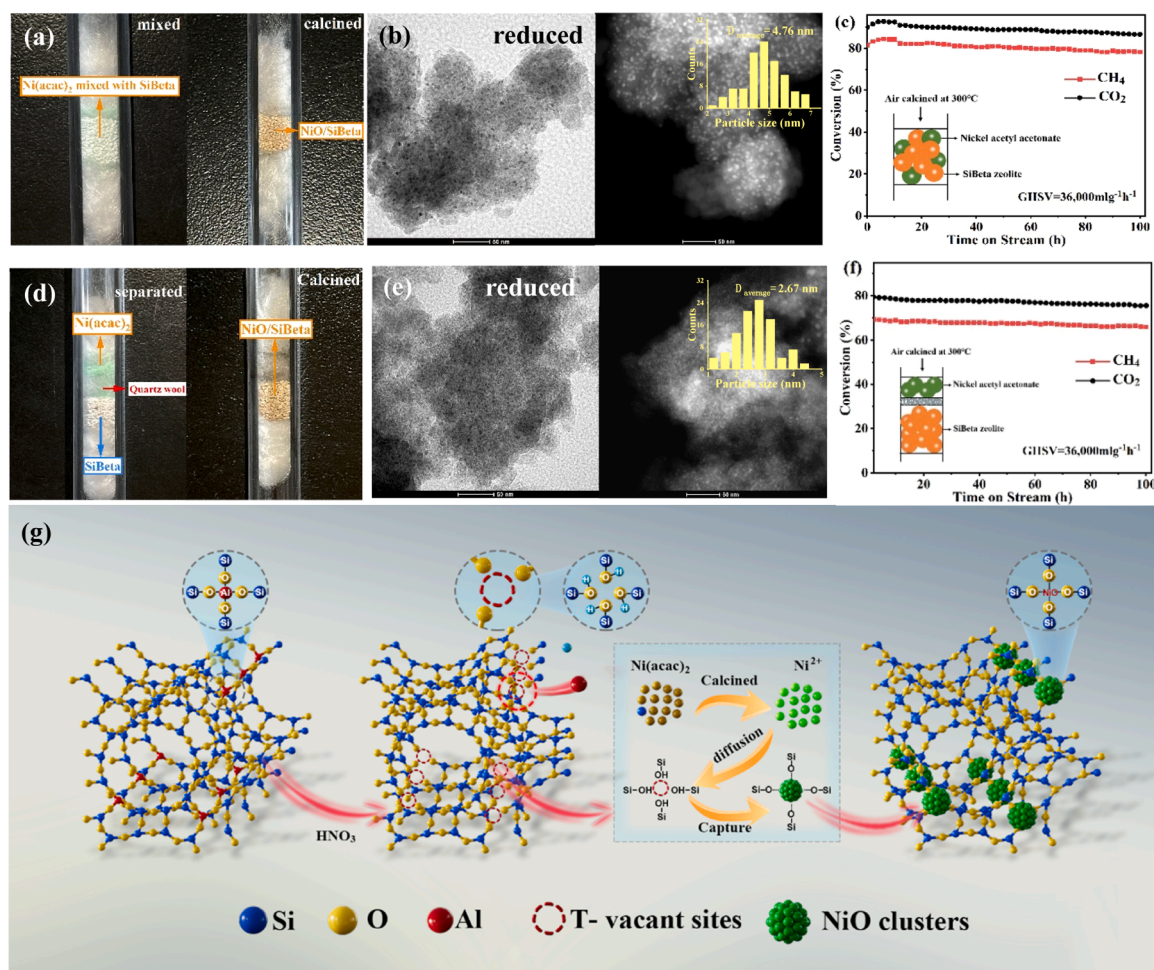


Fig. 2. Photographs, TEM, HAADF-STEM and size distribution as well as DRM performance of Ni/SiBeta-mixed: (a) mixed and calcined, (b) reduced, (c) DRM performance; photographs, TEM, STEM and size distribution as well as DRM performance of Ni/SiBeta-separated: (d) separated and calcined; (e) reduced; (f) DRM performance; and (g) Schematic diagram for the synthesis process of Ni/SiBeta.

the outstanding DRM performance over both designed catalysts, and the excellent DRM stability is maintained in 100 h. Here, the lower actual Ni contents of Ni/SiBeta-Separated is probably owe to exist of the quartz wool, impeding the diffusion of vapor-phase nickel-based precursors during heating process, leading to loss of actual Ni content.

Overall, in this study, Ni/SiBeta catalysts are achieved by anchoring nickel small nanoparticles on T-vacant sites *via* vapor-phase-trapping strategy. This strategy involves two basic steps, as shown in Fig. 2g: (i) removing framework aluminum atoms from the zeolite crystal structure to form abundant silanol nests within T-vacant sites, and (ii) mixing the nickel acetylacetonate precursors with SiBeta zeolites and calcining at 300 °C in air, where the vapor-phase nickel species diffuse into T-vacant sites and are trapped by the silanol nests to yield Ni/SiBeta catalysts. It is worth noting that in this study active Ni species are dynamic trapped *via* the following steps including process of diffusion of nickel precursors, dehydration condensation of hydroxyl sites from silanol nest and the subsequent reduction process at elevated temperature. Similar *in-situ* trap concept on Zn zeolite materials has been reported [48], in that study *in situ* formation of ZnO_x species depends on the constant supplementation of Zn atoms, and then reacting with support OH groups. Besides, dynamic capture is also utilized for copper nanoparticle catalyst [49], where migratable copper sites activated by methanol are trapped by silanol nests of dealuminated Beta zeolite to form nanometer sized Cu particles.

3.3. Physicochemical and structural properties of Ni-based catalysts

In order to explore physicochemical and structural properties of active Ni species on the prepared catalysts, characterizations of UV-vis, H₂ chemisorption, H₂-TPR, quasi *in situ* XPS, X-ray absorption spectroscopy (XAS) experiments, and Pyridine FT-IR spectra are performed. Fig. S6 shows the UV-vis spectrum in the 200–800 nm range, and the oxidation states and coordination of Ni species are investigated. As mentioned above, the signal regions for all catalysts in Fig. 3a are associated with ligand-metal charge transfer (LMCT) bands from the 2p orbital of O²⁻ to the 3d orbital of Ni²⁺. The location of the maximum LMCT value is relevant to the degree of NiO agglomeration [47], and the LMCT order of samples is: Ni/SiO₂ (273 nm) > Ni/HAlBeta (261 nm) > Ni/SiBeta-C (250 nm) > Ni/Al₂O₃ (238 nm) > Ni/SiBeta (235 nm). The results show that the Ni/SiBeta catalyst has the smallest LMCT value, revealing a higher dispersion of NiO on Ni/SiBeta catalyst than other catalysts. Fig. 3b, c further quantifies the dispersion and average particle size of Ni species over catalysts calculated from H₂ chemisorption after reduction. Among all samples, the Ni/SiBeta catalyst has the smallest Ni particles of 3.33 nm and the highest Ni dispersion of 24.1%, indicating anchoring of nickel within T-vacant sites promotes high dispersion of Ni. The Ni/SiBeta-C catalyst shows inferior small Ni particles size of 4.32 nm and Ni dispersion of 18.55%, since less T-vacant sites are present in Ni/SiBeta-C after calcination. In contrast, Ni/HAlBeta catalyst displays large Ni particles of 7.55 nm and low Ni dispersion of 10.62%, due to the deficiency of T-vacant sites. Moreover, the particle size and

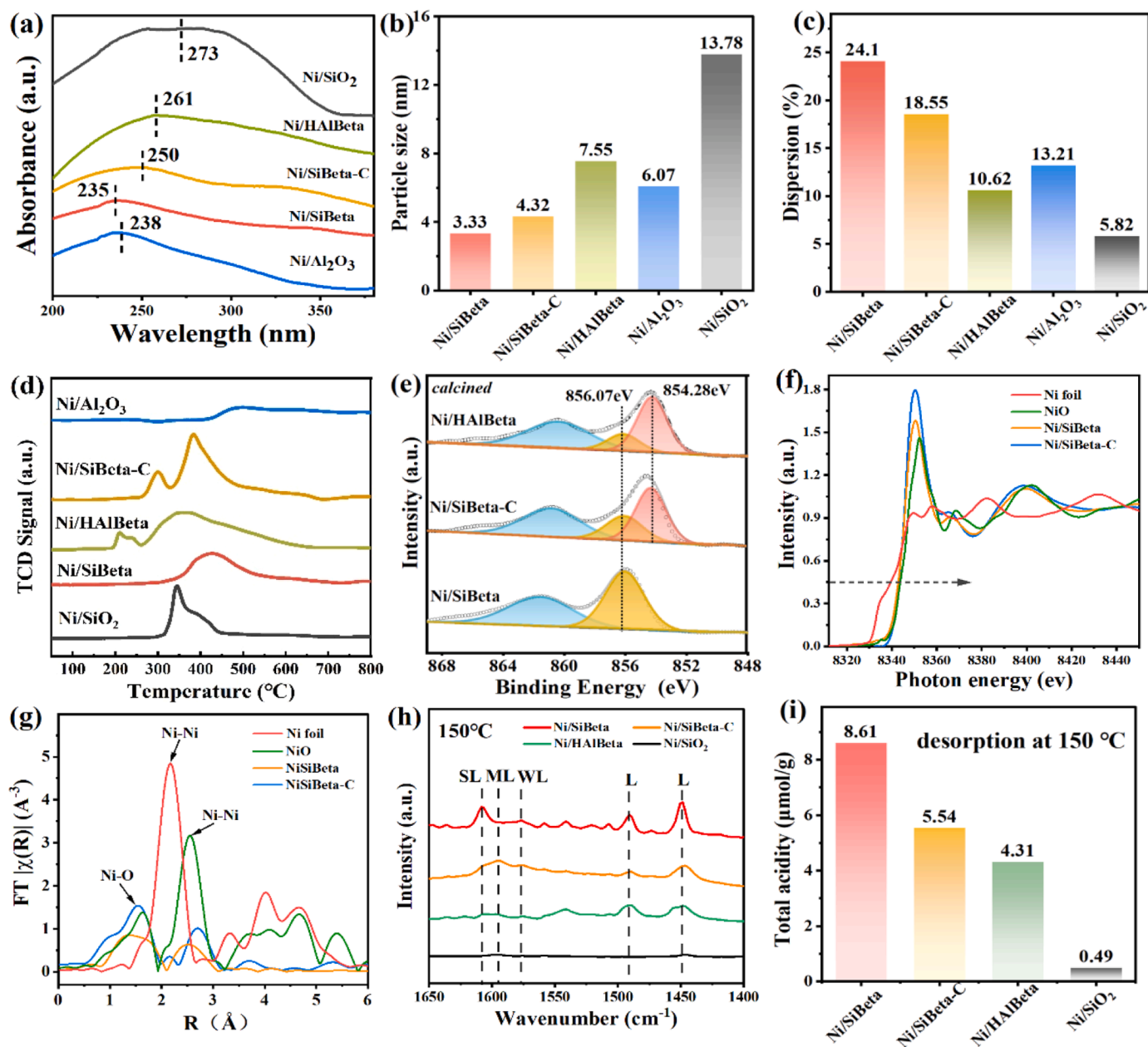


Fig. 3. Characterization of Ni-supported catalysts: (a) UV-vis-DRS of calcined samples, (b-c) comparison of dispersion and mean particle size of reduced catalysts calculated from H₂ chemisorption, (d) H₂-TPR, (e) quasi *in situ* Ni 2p XPS of calcined samples, (f) Ni-K edge XANES spectra and (g) EXAFS Fourier transform of calcined Ni-based SiBeta catalysts with Ni foil and NiO as the references, (h) pyridine IR spectra of calcined catalysts and (i) acidic properties of different catalysts (desorption at 150 °C).

dispersion of Ni over Ni/Al₂O₃ catalyst are 6.07 nm and 13.21%, respectively. The Ni/SiO₂ catalyst reveals the largest Ni particles of 13.78 nm and the lowest Ni dispersion of 5.82%, which is consistent with the results of UV-vis spectrum. Meanwhile, the XRD patterns from Fig. S7 (a-c) and Fig. S8 show that NiO particles obviously agglomerate on the Ni/SiO₂ and Ni/HAlBeta catalysts, while Ni species are well dispersed on Ni/SiBeta catalyst even the Ni content is up to 10%.

The H₂-TPR curves from Fig. 3d can provide key information about the strength of metal-support interaction. In the Ni/SiO₂ catalyst, there is a broad reduction peak located at 344 °C with a weak shoulder peak at 394 °C, corresponding to the reduction of nickel oxide [47], representing weak interactions with the support. For the Ni/Al₂O₃ catalyst, there is a broad reduction peak existed at high-temperature position from 420 °C to 800 °C. Therein, the peaks lower than 600 °C can be ascribed to the reduction of NiO species interacted with the alumina support, and

the higher temperature peaks are attributed to the reduction of formed inactive nickel aluminate phases [50]. The only reduction peak centered at around 425 °C appears in the Ni/SiBeta catalyst, and this behavior can be associated with the reduction of surface Ni silicate species formed by metal-support interaction between small-sized NiO particles and dealuminated beta support [29]. As a result, Ni/SiBeta shows moderate metal-support interaction, and this moderate interaction is strong enough to impede Ni sintering on the support. There are two well separated peaks located at about 300 °C and 387 °C in the Ni/SiBeta-C catalyst. The peak at low temperature is attributed to the reduction of large NiO crystallites (regarded as “free” or “bulk-like” NiO) on the support surface, while the higher temperature-reduction peak is due to the small NiO nanoparticles interacting with T-vacant sites. The appearance of the low temperature peak indicates that the remaining T-vacant sites after calcination are not enough to anchor all NiO. For the

Ni/HAlBeta catalyst, two low-temperature reduction peaks appear at 210 °C and 350 °C, corresponding to the formation of varying NiO species on the support, indicating weak interactions with the support due to the absence of T-vacant sites.

Quasi *in situ* XPS is a suitable method to monitor the interaction of Ni with silanol groups in supports. As mentioned above, capture of Ni sites is actually achieved *via* the process of diffusion of nickel precursors, and dehydration condensation of hydroxyl sites from silanol nest as well as the subsequent reduction process at elevated temperature. Fig. 3e and Fig. S9 displays the quasi *in situ* XPS spectra of calcined Ni/SiBeta, Ni/SiBeta-C and Ni/HAlBeta catalysts after dehydration condensation of hydroxyl sites at 300 °C and subsequent reduction process at 750 °C, respectively. Here, the Ni 2p_{3/2} orbital can be decomposed into two contributions at 854.28 eV and 856.07 eV, attributed to the weak binding of NiO with the support and the strong binding between NiO small-nanoparticles and T-vacant sites, respectively [46]. The Ni/SiBeta catalyst shows only one peak at 856.07 eV, which is assigned to the strong binding between the NiO small-nanoparticles and T-vacant sites within the support. By comparison, low binding energy peak of 854.28 eV appears in Ni/SiBeta-C and Ni/HAlBeta catalysts, indicating the presence of NiO weakly bound to the supports, which fits well with the H₂-TPR results. For subsequent reduced catalysts, both Ni⁰ (852.0–852.3 eV) and Ni²⁺ (about 854 eV) coexist on the surface of all catalysts (Fig. S9), and it is well known that the DRM requires metallic nickel sites rather than positively charged ones for superior activity. The Ni⁰/(Ni⁰ + Ni²⁺) ratio of reduced Ni/SiBeta, Ni/SiBeta-C and Ni/HAlBeta is 0.60, 0.65, and 0.69. The decrease of Ni⁰ content in Ni/SiBeta can be attributed to the strong metal-support binding, which reduces the reducibility of Ni/SiBeta. Besides, it is believed that the stronger nickel species interacts with silica, the more the peaks are shifted to higher energy value [51]. Here, the shift of Ni⁰ peak for Ni/SiBeta to higher energy values proves again that Ni/SiBeta possesses the stronger metal-support interaction.

Coordination numbers, adjacent atoms, and bond distances of Ni chemical environment are determined by XAS analysis [52,53]. Fig. 3f, g compares the XANES and EXAFS spectra of Ni foil, NiO, Ni/SiBeta and Ni/SiBeta-C catalysts. Fig. 3f shows that the absorption edge energies of Ni/SiBeta and Ni/SiBeta-C are closer to those of NiO, indicating that the Ni species in the calcined catalyst is in the form of NiO. The corresponding EXAFS wavelet transform (WT) analysis are shown in Fig. S10, the signals of 4.08 Å⁻¹ and 6.98 Å⁻¹ appeared in both Ni/SiBeta and Ni/SiBeta-C are consistent with the Ni-O and Ni-Ni paths, further confirming that Ni species exist in the formation of NiO after calcination. The FTs of the EXAFS spectra with phase correlation are shown in Fig. 3g, and the structural parameters obtained from the EXAFS spectra (Fig. S11) are displayed in Table S2. From Fig. 3g, the position of the Ni-Ni scattering path presented in the second shell at 2.5 Å towards the Ni/SiBeta is similar to that of NiO, while its intensity is lower than that of reference NiO, suggesting the high dispersion and small nanoparticle size of NiO on the Ni/SiBeta. Moreover, the coordination numbers are determined to be 6.2 and 7.1 for the Ni/SiBeta-C catalyst in the first and second shells, while 5.2 and 5.5 are respectively obtained for the Ni/SiBeta catalyst. Obviously, the small NiO nanoparticles in the Ni/SiBeta show smaller coordination number than that of the Ni/SiBeta-C, implying the NiO in the Ni/SiBeta catalyst forms small-nanoparticles due to the presence of abundant T-vacant sites and possess a higher proportion of undercoordinated surface atoms [54].

In general, Lewis acid sites are usually thought to be caused by the unsaturated coordination metal sites. The lower number of metal coordination sites, the higher amount of Lewis acid sites is exhibited. Pyridine FT-IR spectra and quantitative Lewis acid numbers of catalysts are shown in Fig. 3h, i (desorption at 150 °C) and Fig. S12a, b (desorption at 400 °C). In Fig. 3h and Fig. S12a, there are five bands to represent the presence of the Lewis acidic sites, with the strong intensity peak at 1449 cm⁻¹, the weak peak located at 1490 cm⁻¹, and a broad peak in the range from 1570 to 1630 cm⁻¹ consisting of Lewis acids with various

strengths, namely, the peak at 1608 cm⁻¹ belongs to strong Lewis (SL) acid site, and the peak at 1595 cm⁻¹ results from moderately strong Lewis (mL) acid site, while the peak at 1575 cm⁻¹ attributes to weak Lewis (mL) acid [55]. Among all the catalysts, the Ni/SiBeta catalyst records the highest amount of Lewis acid sites (Fig. 3i and Fig. S12b), with quantitative acid amount of 8.61 μmol/g at 150 °C and 6.15 μmol/g at 400 °C, while the acid amount of Ni/SiBeta-C are 5.54 μmol/g and 2.46 μmol/g at 150 °C and 400 °C, respectively. For the Ni/HAlBeta and Ni/SiO₂ samples, they exhibit much low amount of Lewis acid sites. This result is in agreement with the findings of the XAS, in which the lower average coordination number of NiO small nanoparticles causes the higher amount of Lewis acid sites.

According to above results, it is well accepted that trapped nickel species *via* vapor-phase-trapping strategy show high dispersion and moderate metal-support interaction, thus improving nickel utilization efficiency. Therefore, high DRM performance over the Ni/SiBeta catalyst is expected.

3.4. Catalytic performance for DRM

The catalytic performance of DRM over these Ni-based catalysts (including traditional Ni/Al₂O₃ and Ni/SiO₂ catalysts for comparison) is subjected at 750 °C, GHSV = 100,000 mLg⁻¹h⁻¹ for 100 h of test (Fig. 4a, b). As can be seen from Fig. 4a, the Ni/SiBeta catalyst shows the highest conversion of reactants (X_{CH₄}=76.5% and X_{CO₂}=83.2%) and outstanding catalytic stability, illustrating the superior nickel utilization and good stability over the present catalyst. The initial conversion of CH₄ and CO₂ on the Ni/SiBeta-C catalyst is 62.7% and 71.4%, respectively, and maintains inferior catalytic stability during 100h of test. By comparison, the prime conversion rate of CH₄ and CO₂ on Ni/HAlBeta samples are only 48.2% and 54.7%, and severe deactivation occurs during the 20 h of reaction. For the traditional Ni/Al₂O₃ catalyst, the initial conversion rate of CH₄ and CO₂ are only 59.3% and 69.2%, and the conversion rate of CH₄ and CO₂ drops significantly after 100 h of reaction. This is probably because Ni/Al₂O₃ forms overly stable NiAl₂O₄ during the calcination process, which reduces the exposure of active metals. Ni/SiO₂ catalyst shows high catalytic activity at the beginning of the reaction, with initial conversions of CH₄ and CO₂ are 67.2% and 78.3%. However, the active metals on Ni/SiO₂ are unstable, and the catalyst deactivation is much serious after 100 h of reaction. Furthermore, Fig. S13 shows the value of H₂/CO, and the Ni/SiBeta catalyst exhibits the highest H₂/CO. Besides, the TOF values and stability of different DRM catalysts from the reported literature and the present work are compared in Fig. S14a, b and Tables S3 and S4, which indicates that the currently developed catalysts have superior catalytic reactivity.

In order to further understand the catalytic performance of the prepared catalysts for DRM reaction, discussions regarding CH₄-TPSR, CO₂-TPD and apparent activation energy analysis are carried out. The CH₄-TPSR is given in Fig. 4c, where the activation decomposition of CH₄ in the Ni/SiBeta catalyst starts at 318 °C and reaches a maximum at 547 °C, indicating that Ni/SiBeta catalyst is extremely capable of activating CH₄. In comparison to the Ni/SiBeta catalyst, Ni/SiBeta-C also shows two CH₄ activation peaks, but requires high activation temperature. For the Ni/HAlBeta, NiAl₂O₃ and Ni/SiO₂ catalysts, only one high temperature peak is observed, at 601 °C, 556 °C and 594 °C respectively, indicating that the latter three catalysts are less capable of activating CH₄, corresponding to their DRM catalytic performance as shown in Fig. 4a, b. In the apparent activation energy experiments from Fig. 4d, the pattern of CH₄ activation capacity is confirmed again. The specific calculation of the activation energy for each catalyst is shown in Fig. S15. The calculated value of apparent activation energies (E_a) for these catalysts in this study is in the range of reported activation energy for DRM on various Ni-based catalysts, which typically lies between 33–100 kJ/mol [14,35,56], and compared to apparent activation energies value (above 50 kJ) of other catalysts in most of literatures, that of designed catalyst in this paper is lower (around 40 kJ/mol). The order of

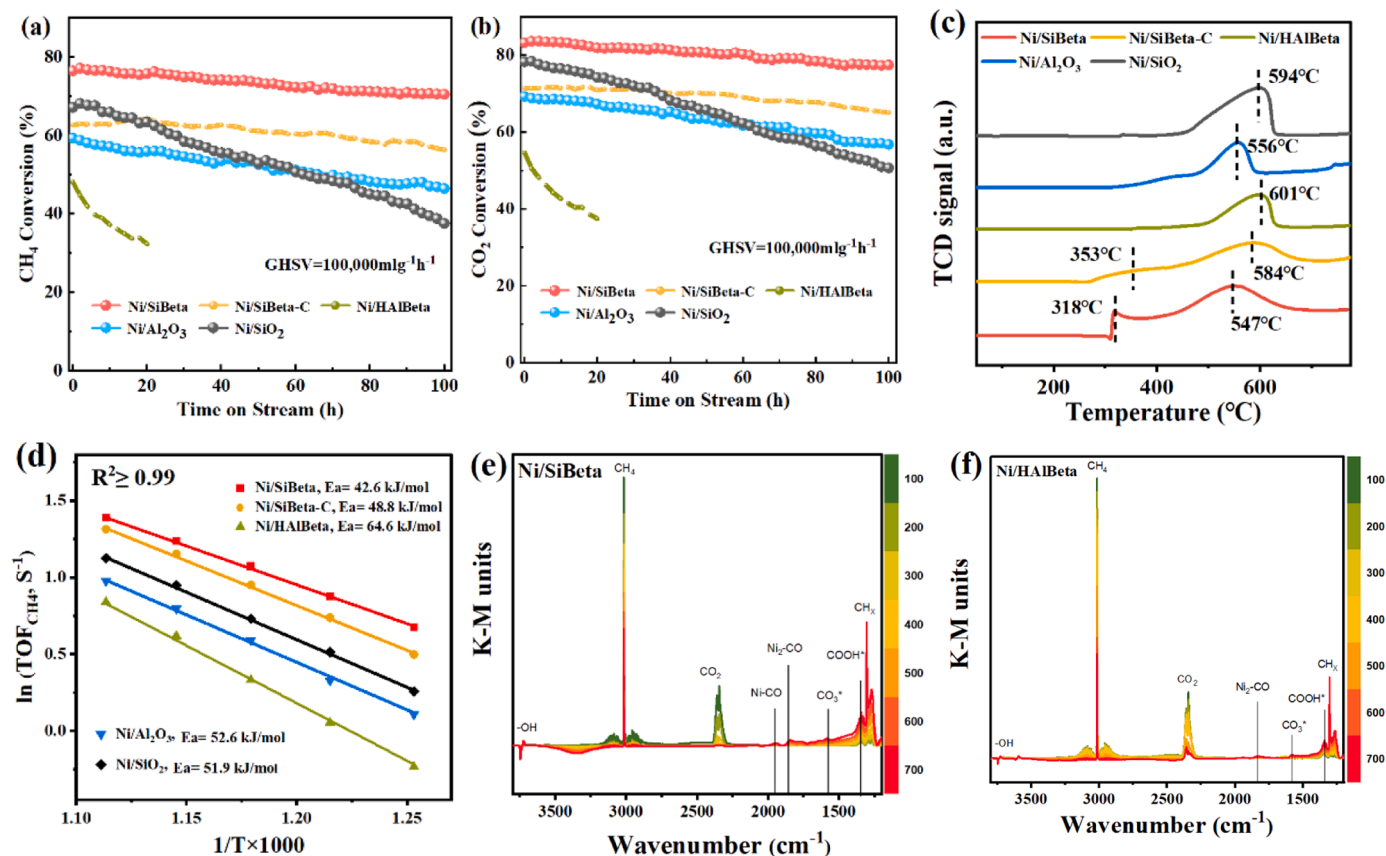


Fig. 4. (a) CH₄ and (b) CO₂ conversion for five catalysts under high GHSV conditions for 100 h of continuous reaction (reaction conditions: $m_{\text{catalyst}} = 60$ mg, CH₄/CO₂/N₂ = 1/1/1, $T_{\text{reduction}} = 750$ °C, $T_{\text{reaction}} = 750$ °C, GHSV = 1 00000 mL·h⁻¹·gcat⁻¹), (c) CH₄-TPSR analysis, (d) arrhenius plots for CH₄ activation energies (reaction conditions: $m_{\text{catalyst}} = 10$ mg, CH₄/CO₂/N₂ = 1/1/1, $T_{\text{reduction}} = 750$ °C, GHSV = 600,000 mL·h⁻¹·gcat⁻¹), and *in situ* CH₄ + CO₂-DRIFT spectra of (e) Ni/SiBeta and (f) Ni/HAlBeta.

CH₄ activation capacity here is: Ni/SiBeta > Ni/SiBeta-C > Ni/SiO₂ > Ni/Al₂O₃ > Ni/HAlBeta. In addition, CO₂-TPD experiments are performed to understand the CO₂ adsorption capacity of catalysts. In general, the higher adsorption temperature and larger peak area correspond to the stronger CO₂ adsorption capacity of catalysts [57]. As shown in Fig. S16, Ni/SiBeta and Ni/SiBeta-C catalysts have adsorption peaks in close proximity at approximately 320 °C, but the Ni/SiBeta catalyst has a more intense peak and is more capable of adsorbing CO₂. The adsorption peak of Ni/HAlBeta appears at a low temperature of 170 °C, indicating its weak capacity for CO₂ adsorption. The Ni/SiO₂ shows a very weak peak, implying a weaker CO₂ adsorption ability. Therefore, the results of CO₂-TPD and CH₄-TPSR consistently prove that Ni/SiBeta has the best activation ability for the reactant gases of CH₄ and CO₂.

In-situ CH₄/CO₂-DRIFTS are conducted and displayed in Fig. 4e, f, and Fig. S17. For CH₄ adsorption over two reduced samples (Ni/SiBeta and Ni/HAlBeta in Fig. S17 a, c), the band at 3016 cm⁻¹ corresponds to absorbed CH₄. Simultaneously, the band appeared at 1342 cm⁻¹ is attributed to the deformation vibration of CH_x. It is noted that, different from observed band intensity of CH_xO intermediate species at 1052 cm⁻¹ over Ni/Al₂O₃ system in previous report [17], in this study the IR bands of formate species and bidentate carbonates at 1376 cm⁻¹ and 1543 cm⁻¹ are detected, respectively [14]. In addition, other two peaks at 1950 cm⁻¹ and 1880 cm⁻¹ are respectively attributed to bridged and multi-centered CO on metal Ni [58]. What is striking is that the peak intensity of CH_x, formate, carbonates as well as CO gradual increases along with gradual decomposition of CH₄ with the increase of temperature, indicating that CH₄ activation and decomposition can be induced by the small sized metallic Ni active sites *via* forming CH_x species, carbonates as well as formates, consistent with the result in

literature [14]. It is observed that the intensity of the above species over the Ni/SiBeta is stronger than that over the Ni/HAlBeta, indicating the enhanced CH₄ activation capacity for Ni/SiBeta, corresponding to CH₄-TPSR results and apparent activation energy analyses. Furthermore, in terms of CO₂ adsorption on the reduced samples (Fig. S17 b, d) CO₂ activation also could be evoked by nanometer-scale nickel metal *via* formation of carbonates and formates adsorbed on the support or the interface between metallic Ni active sites and the support with the help of H species [14]. Here, the peak intensity ascribed to carbonate, formates, and CO species over the Ni/SiBeta is stronger than that over the Ni/HAlBeta catalyst, implying that Ni/SiBeta exhibits stronger CO₂ adsorption capacity, corresponding to the result of CO₂-TPD. When CO₂ and CH₄ are introduced together (Fig. 4e, f), higher characteristic peaks for the mentioned intermediates during DRM reaction is found over the Ni/SiBeta. Overall, T-vacant sites within beta zeolite support can dynamically trap Ni species to obtain highly dispersed and small-size Ni nanoparticles, and these Ni nanoparticles can activate methane and CO₂, finally achieving the balance between the activation of CH₄ and CO₂. On the basis of the results obtained by *in-situ* DRIFTS, the basic reaction steps demonstrated in Fig. S18 seem appropriate to describe the DRM reaction mechanism on Ni/SiBeta.

To understand the reason for the difference in the activity of each catalyst and the cause for the deactivation, TEM and different HAADF-STEM regions over all fresh and spent samples are performed. Firstly, TEM and HAADF-STEM images of Ni/SiBeta catalyst are displayed in Fig. 5a, b. The average size of Ni particles in the fresh sample is only 2.85 nm, which is close to the result of H₂ chemisorption (Fig. 3b). After 100 h of reaction at high temperature, the Ni particle size only increases to 4.39 nm (Fig. 5c, d), indicating that Ni/SiBeta has an excellent ability

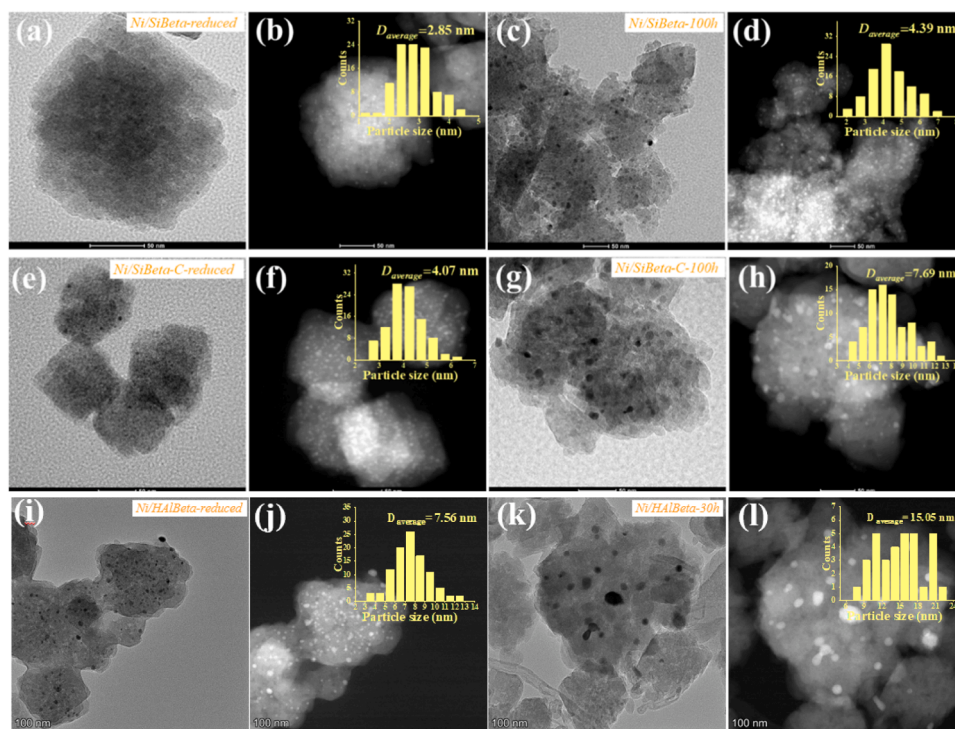


Fig. 5. TEM, HAADF-STEM images and corresponding size distributions of the catalysts: (a, b) reduced Ni/SiBeta, (c, d) spent Ni/SiBeta, (e, f) reduced Ni/SiBeta-C, (g, h) spent Ni/SiBeta-C, (i, j) reduced Ni/HAlBeta, (k, l) spent Ni/HAlBeta.

to prevent sintering. The fresh Ni/SiBeta-C catalyst in Fig. 5e, f exhibits larger Ni particles of 4.07 nm, which increases to 7.69 nm after 100 h of reaction (Fig. 5g, h). Ni/SiBeta-C exhibits slightly

larger Ni size and weaker ability to avoid sintering, because the decreased T-vacant sites after calcination cannot afford complete anchoring of Ni, causing weakened metal-support interaction, which has been proved by above characterization results. In Ni/HAlBeta catalyst, the average size of Ni particles over fresh sample is 7.56 nm (Fig. 5i, j), which is in agreement with the results of H_2 chemisorption (Fig. 3b). However, the Ni/HAlBeta catalyst undergoes severe sintering after just 30 h of reaction (Fig. 5k, l), with the Ni particles growing to 15.05 nm, due to the absence of T-vacant sites on the HAlBeta support. Fig. S19 shows the TEM and HAADF-STEM images of Ni/Al₂O₃, and no larger Ni particles are observed before and after the reaction, while the Ni particles of the Ni/SiO₂ catalyst increase from 15.48 nm to 34.35 nm after 100 h of reaction, due to the weak interactions between metal species and support (Fig. S20). Besides, the TG and DTG curves of catalysts after reaction are exhibited in Fig. S22. All catalysts, except Ni/SiO₂ catalyst, show little amount of carbon deposition, especially Ni/SiBeta catalyst, in which the carbon balance maintains around 1.0 during DRM reaction for 100 h and there is no carbon sign in catalyst's photographs after reaction, as shown in Fig. S23 and Fig. S26. Combined with the results of DRM performance in Fig. 4a, b, we suggest that the main cause of catalyst deactivation here is not carbon deposition, but active metal sintering, and Ni/SiBeta catalyst prepared via vapor-phase-trapping strategy possesses superior tolerance behavior.

3.5. Comparison of dynamic trap strategy and traditional impregnation method

In the end, in order to further confirm the advantage of dynamic trap strategy, a series of characterizations as well as DRM performance test over Ni/SiBeta-I catalyst, prepared by traditional impregnation method but on the same SiBeta support as the Ni/SiBeta catalyst, are performed. Small angle XRD patterns, N_2 adsorption-desorption and BET data of both nickel based catalysts in Fig. S24 and Table S5 firstly display that

the crystal and skeleton structure of Beta zeolite have no significant disruption or loss after high-temperature reaction at 750 °C. However, in Fig. S25 the conversion rate of CH₄ and CO₂ over Ni/SiBeta-I catalyst decreases obviously after 100 h of reaction, compared to that over Ni/SiBeta. It is worth noting that the Ni/SiBeta-I catalyst possesses 11.50 nm of particle size (Fig. S21 a, b), which is much larger than that of the Ni/SiBeta catalyst (2.85 nm), indicating that the traditional impregnation method does not afford suitable strategy for Ni species to be highly dispersed on the SiBeta support, even containing ample T-vacant sites. In addition, the Ni/SiBeta-I catalyst undergoes significantly sintering after 100 h DRM reaction (Fig. S21 c, d), with the Ni particles growing to 32.14 nm, and also generates more amount of carbon deposition, as shown in Fig. S26. By contrast, in vapor-phase-trapping strategy, nickel acetylacetonate diffuses into the SiBeta support with abundant silanol nests, and the T-vacant sites trap Ni species and form small-sized and highly dispersed NiO nanoparticles, exhibiting outstanding DRM performance. For slight deactivation over Ni/SiBeta after DRM reaction, although the conversion of CH₄ and CO₂ over Ni/SiBeta in this study drops about 3% during DRM test in Fig. 4a, b, this reaction is at high temperature (750 °C), long-term operation (100 h) and under the condition of quite high GHSV (100,000 mL·g⁻¹·h⁻¹) compared to other supported nickel catalysts in literatures, as shown in Fig. S14 and Table S4, in which trace amount of deactivation is unavoidable [59–61]. In view of particle sintering over Ni/SiBeta after DRM reaction in Fig. 5(a–c), the recent relevant literatures summarized in Fig. S27 and Table S6 clearly show that particle sintering is the same unavoidable during DRM reaction especially under severe reaction condition of high temperature, long-term operation and high GHSV condition. It is worth noting that our developed catalyst possesses enough small-size nanoparticles (2.85 nm) in a wide scope of literatures, and displays superior catalytic stability even under the condition of quite high GHSV (100,000 mL·g⁻¹·h⁻¹). More importantly, nickel nanoparticles of Ni/SiBeta in this study still maintain fairly small sizescale (4.39 nm) [62] after DRM reaction in 750 °C for 100 h. By comparison, it is obvious that the designed catalyst in this study has reached top-level nickel catalysts with superior durability and tolerance

among many studies. As a result, the dynamic trap strategy at elevated temperature provides applicability for the synthesis of high-efficiency heterogeneous catalyst within small nanoparticles. Yunnan Major Scientific and Technological Projects (Grant No. 202302AG050002).

4. Conclusion

In summary, a novel vapor-phase-trapping strategy is proposed in this study to design and synthesize BEA zeolite supported DRM catalyst with superior nickel utilization. Through transferring nickel-based precursors in vapor phase into the silanol nests of dealuminated Beta zeolite at high temperature, Ni small nanoparticles are stably anchored in silanol nests to achieve dynamic trap of nickel components. More importantly, such Ni sites achieve high dispersion and establish moderate interaction within the dealuminated zeolite BEA support, showing dual-role of anchoring active Ni sites and benefiting outstanding DRM performance. We suppose that the present strategy applied to trap active nickel small nanoparticles is possibly applied for other heterogeneous reactions.

CRedit authorship contribution statement

Cao Xiaohua: Validation. **Wu Shaojie:** Formal analysis, Investigation. **He Dedong:** Conceptualization, Data curation, Funding acquisition, Resources, Supervision, Validation, Writing – review & editing. **Zhang Lei:** Investigation, Validation. **Chen Dingkai:** Formal analysis, Supervision, Validation, Writing – original draft, Writing – review & editing. **luo yongming:** Funding acquisition, Supervision, Validation. **Zhang Yu:** Data curation, Validation.

Declaration of Competing Interest

The authors declare that they have no known competing financial interests or personal relationships that could have appeared to influence the work reported in this paper.

Data availability

Data will be made available on request.

Acknowledgments

The authors wish to acknowledge the financial support provided by the National Natural Science Foundation of China (22006059, 21968015, 22208136, 42030712, 21966018), Excellent Youth Project of Natural Science Foundation of Yunnan Province (202201AW070007), Young Academic and Technical Leader Raising Foundation of Yunnan Province (202205AC160011), Key Project of Natural Science Foundation of Yunnan Province (No. 202101AS070026), and Yunnan Major Scientific and Technological Projects (Grant No. 202302AG050002, 202202AG050001-5).

Appendix A. Supporting information

Supplementary data associated with this article can be found in the online version at [doi:10.1016/j.apcatb.2024.123728](https://doi.org/10.1016/j.apcatb.2024.123728).

References

- [1] X. Chen, X. Qin, Y. Jiao, M. Peng, J. Diao, P. Ren, C. Li, D. Xiao, X. Wen, Z. Jiang, N. Wang, X. Cai, H. Liu, D. Ma, Structure-dependence and metal-dependence on atomically dispersed Ir catalysts for efficient n-butane dehydrogenation, *Nat. Commun.* 14 (2023) 1–11, <https://doi.org/10.1038/s41467-023-38361-4>.
- [2] Y. Tian, H. Duan, B. Zhang, S. Gong, Z. Lu, L. Dai, C. Qiao, G. Liu, Y. Zhao, Y. J. Tian, H.N. Duan, C.Z. Qiao, L. Dai, Y. Zhao, B.F. Zhang, S.Y. Gong, Z.J. Lu, G. Z. Liu, Template guiding for the encapsulation of uniformly subnanometric platinum clusters in beta-zeolites enabling high catalytic activity and stability, *Angew. Chem. Int. Ed.* 60 (2021) 21713–21717, <https://doi.org/10.1002/ANGE.202108059>.
- [3] Y. Liu, Y. Chen, Z. Gao, X. Zhang, L. Zhang, M. Wang, B. Chen, Y. Diao, Y. Li, D. Xiao, X. Wang, D. Ma, C. Shi, Embedding high loading and uniform Ni nanoparticles into silicalite-1 zeolite for dry reforming of methane, *Appl. Catal. B Environ.* 307 (2022) 121202, <https://doi.org/10.1016/j.apcatb.2022.121202>.
- [4] H. Wang, Y. Diao, Z. Gao, K.J. Smith, X. Guo, D. Ma, C. Shi, H₂ production from methane reforming over molybdenum carbide catalysts: from surface properties and reaction mechanism to catalyst development, *ACS Catal.* 12 (2022) 15501–15528, https://doi.org/10.1021/ACSCATAL.2C04619/ASSET/IMAGES/LARGE/CS2C04619_0015.JPEG.
- [5] L. Cao, W. Liu, Q. Luo, R. Yin, B. Wang, J. Weissenrieder, M. Soldemo, H. Yan, Y. Lin, Z. Sun, C. Ma, W. Zhang, S. Chen, H. Wang, Q. Guan, T. Yao, S. Wei, J. Yang, J. Lu, Atomically dispersed iron hydroxide anchored on Pt for preferential oxidation of CO in H₂, *Nat* 565 (2019) 631–635, <https://doi.org/10.1038/s41586-018-0869-5>.
- [6] Y. Yao, X. Wu, O.Y. Gutiérrez, J. Ji, P. Jin, S. Wang, Y. Xu, Y. Zhao, S. Wang, X. Ma, J.A. Lercher, Roles of Cu⁺ and Cu⁰ sites in liquid-phase hydrogenation of esters on core-shell CuZn_x@C catalysts, *Appl. Catal. B Environ.* 267 (2020) 118698, <https://doi.org/10.1016/j.apcatb.2020.118698>.
- [7] Q. Jiang, Y. Liu, T. Dintzer, J. Luo, K. Parkhomenko, A.C. Roger, Tuning the highly dispersed metallic Cu species via manipulating Brønsted acid sites of mesoporous aluminosilicate support for CO₂ hydrogenation reactions, *Appl. Catal. B Environ.* 269 (2020) 118804, <https://doi.org/10.1016/j.apcatb.2020.118804>.
- [8] R. Lang, W. Xi, J.C. Liu, Y.T. Cui, T. Li, A.F. Lee, F. Chen, Y. Chen, L. Li, L. Li, J. Lin, S. Miao, X. Liu, A.Q. Wang, X. Wang, J. Luo, B. Qiao, J. Li, T. Zhang, Non defect-stabilized thermally stable single-atom catalyst, *Nat. Commun.* 10 (2019) 1–10, <https://doi.org/10.1038/s41467-018-08136-3>.
- [9] Z. Yang, B. Chen, W. Chen, Y. Qu, F. Zhou, C. Zhao, Q. Xu, Q. Zhang, X. Duan, Y. Wu, Directly transforming copper (I) oxide bulk into isolated single-atom copper sites catalyst through gas-transport approach, *Nat. Commun.* 10 (2019) 1–7, <https://doi.org/10.1038/s41467-019-11796-4>.
- [10] Q. Sun, N. Wang, Q. Fan, L. Zeng, A. Mayoral, S. Miao, R. Yang, Z. Jiang, W. Zhou, J. Zhang, T. Zhang, J. Xu, P. Zhang, J. Cheng, D.C. Yang, R. Jia, L. Li, Q. Zhang, Y. Wang, O. Terasaki, J. Yu, Subnanometer bimetallic platinum–zinc clusters in zeolites for propane dehydrogenation, *Angew. Chem. Int. Ed.* 59 (2020) 19450–19459, <https://doi.org/10.1002/ANGE.202003349>.
- [11] L. Liu, M. Lopez-Haro, C.W. Lopes, S. Rojas-Buzo, P. Concepcion, R. Manzorro, L. Simonelli, A. Sattler, P. Serna, J.J. Calvino, A. Corma, Structural modulation and direct measurement of subnanometric bimetallic PtSn clusters confined in zeolites, *Nat. Catal.* 3 (2020) 628–638, <https://doi.org/10.1038/s41929-020-0472-7>.
- [12] H. Jeong, O. Kwon, B.S. Kim, J. Bae, S. Shin, H.E. Kim, J. Kim, H. Lee, Highly durable metal ensemble catalysts with full dispersion for automotive applications beyond single-atom catalysts, *Nat. Catal.* 3 (2020) 368–375, <https://doi.org/10.1038/s41929-020-0427-z>.
- [13] K. Murata, Y. Mahara, J. Ohyama, Y. Yamamoto, S. Arai, A. Satsuma, The metal-support interaction concerning the particle size effect of Pd/Al₂O₃ on methane combustion, *Angew. Chem.* 129 (2017) 16209–16213, <https://doi.org/10.1002/ANGE.201709124>.
- [14] S. Zhang, M. Ying, J. Yu, W. Zhan, L. Wang, Y. Guo, Y. Guo, Ni₃Al₂O_{7.5} mesoporous catalysts for dry reforming of methane: the special role of NiAl₂O₄ spinel phase and its reaction mechanism, *Appl. Catal. B Environ.* 291 (2021) 120074, <https://doi.org/10.1016/j.apcatb.2021.120074>.
- [15] S. Zhang, L. Tang, J. Yu, W. Zhan, L. Wang, Y. Guo, Y. Guo, Spherical Ni nanoparticles supported by nanosheet-assembled Al₂O₃ for dry reforming of CH₄: elucidating the induction period and its excellent resistance to coking, *ACS Appl. Mater. Interfaces* 13 (2021) 58605–58618, <https://doi.org/10.1021/ACSAMI.1C17890>.
- [16] Y. Chen, S. Ji, C. Chen, Q. Peng, D. Wang, Y. Li, Single-atom catalysts: synthetic strategies and electrochemical applications, *Joule* 2 (2018) 1242–1264, <https://doi.org/10.1016/j.joule.2018.06.019>.
- [17] Y. Zhang, Y. Zu, D. He, J. Liang, L. Zhu, Y. Mei, Y. Luo, The tailored role of “defect” sites on γ-alumina: a key to yield an efficient methane dry reforming catalyst with superior nickel utilization, *Appl. Catal. B Environ.* 315 (2022) 121539, <https://doi.org/10.1016/j.apcatb.2022.121539>.
- [18] Z. Huang, D. He, W. Deng, G. Jin, K. Li, Y. Luo, Illustrating new understanding of adsorbed water on silica for inducing tetrahedral cobalt (III) for propane dehydrogenation, *Nat. Commun.* 14 (2023) 1–11, <https://doi.org/10.1038/s41467-022-35698-0>.
- [19] N.J. LiBretto, Y. Xu, A. Quigley, E. Edwards, R. Nargund, J.C. Vega-Vila, R. Caulkins, A. Saxena, R. Gounder, J. Greeley, G. Zhang, J.T. Miller, Olefin oligomerization by main group Ga³⁺ and Zn²⁺ single site catalysts on SiO₂, *Nat. Commun.* 12 (2021) 1–9, <https://doi.org/10.1038/s41467-021-22512-6>.
- [20] R. ZHANG, G. XIA, M. LI, Y. WU, H. NIE, D. LI, Effect of support on the performance of Ni-based catalyst in methane dry reforming, *J. Fuel Chem. Technol.* 43 (2015) 1359–1365, [https://doi.org/10.1016/S1872-5813\(15\)30040-2](https://doi.org/10.1016/S1872-5813(15)30040-2).
- [21] N. Wang, Q. Sun, J. Yu, N. Wang, Q. Sun, J. Yu, Ultrasmall metal nanoparticles confined within crystalline nanoporous materials: a fascinating class of nanocatalysts, *Adv. Mater.* 31 (2019) 1803966, <https://doi.org/10.1002/ADMA.201803966>.
- [22] J. Zhang, L. Wang, B. Zhang, H. Zhao, U. Kolb, Y. Zhu, L. Liu, Y. Han, G. Wang, C. Wang, D.S. Su, B.C. Gates, F.S. Xiao, Sinter-resistant metal nanoparticle catalysts achieved by immobilization within zeolite crystals via seed-directed growth, 2018 17, *Nat. Catal.* 1 (2018) 540–546, <https://doi.org/10.1038/s41929-018-0098-1>.

- [23] R. Ryoo, J. Kim, C. Jo, S.W. Han, J.C. Kim, H. Park, J. Han, H.S. Shin, J.W. Shin, Rare-earth–platinum alloy nanoparticles in mesoporous zeolite for catalysis, *Nature* 585 (2020) 221–224, <https://doi.org/10.1038/s41586-020-2671-4>.
- [24] L. Qi, M. Babucci, Y. Zhang, A. Lund, L. Liu, J. Li, Y. Chen, A.S. Hoffman, S.R. Bare, Y. Han, B.C. Gates, A.T. Bell, Propane dehydrogenation catalyzed by isolated Pt atoms in $\text{SiO}_2\text{Zn-OH}$ nests in dealuminated zeolite beta, *J. Am. Chem. Soc.* 143 (2021) 21364–21378, https://doi.org/10.1021/JACS.1C10261/ASSET/IMAGES/MEDIUM/JA1C10261_M007.GIF.
- [25] Y. Wang, Z.P. Hu, X. Lv, L. Chen, Z.Y. Yuan, Ultrasmall PtZn bimetallic nanoclusters encapsulated in silicalite-1 zeolite with superior performance for propane dehydrogenation, *J. Catal.* 385 (2020) 61–69, <https://doi.org/10.1016/J.JCAT.2020.02.019>.
- [26] L. Rochlitz, K. Searles, J. Alfke, D. Zemlyanov, O.V. Safonova, C. Copéret, Silica-supported, narrowly distributed, subnanometric Pt–Zn particles from single sites with high propane dehydrogenation performance, *Chem. Sci.* 11 (2020) 1549–1555, <https://doi.org/10.1039/C9SC05599A>.
- [27] Y. Yue, J. Fu, C. Wang, P. Yuan, X. Bao, Z. Xie, J.M. Basset, H. Zhu, Propane dehydrogenation catalyzed by single Lewis acid site in Sn-Beta zeolite, *J. Catal.* 395 (2021) 155–167, <https://doi.org/10.1016/j.jcat.2020.12.019>.
- [28] W. Dai, Q. Lei, G. Wu, N. Guan, M. Hunger, L. Li, Spectroscopic Signature of Lewis Acidic Framework and Extraframework Sn Sites in Beta Zeolites, 2020. (<https://doi.org/10.1021/acscatal.0c02356>).
- [29] W. Gac, M. Greluk, G. Slowik, Y. Millot, L. Valentin, S. Dzwigaj, Effects of dealumination on the performance of Ni-containing BEA catalysts in bioethanol steam reforming, *Appl. Catal. B Environ.* 237 (2018) 94–109, <https://doi.org/10.1016/j.apcatb.2018.05.040>.
- [30] C. Chen, S. Zhang, Z. Wang, Z. Yuan, Ultrasmall Co confined in the silanols of dealuminated beta zeolite: a highly active and selective catalyst for direct dehydrogenation of propane to propylene, *J. Catal.* 383 (2020) 77–87, <https://doi.org/10.1016/j.jcat.2019.12.037>.
- [31] Z. Xu, Y. Yue, X. Bao, Z. Xie, H. Zhu, Propane dehydrogenation over Pt clusters localized at the Sn single-site in zeolite framework, *ACS Catal.* 10 (2020) 818–828, <https://doi.org/10.1021/acscatal.9b03527>.
- [32] A. Wong, Q. Liu, S. Griffin, A. Nicholls, J.R. Regalbuto, Synthesis of ultrasmall, homogeneously alloyed, bimetallic nanoparticles on silica supports, *Science* 358 (80) (2017) 1427–1430, <https://doi.org/10.1126/science.aao6538>.
- [33] H. Xiong, D. Kunwar, D. Jiang, C.E. Garcia-Vargas, H. Li, C. Du, G. Canning, X. I. Pereira-Hernandez, Q. Wan, S. Lin, S.C. Purdy, J.T. Miller, K. Leung, S.S. Chou, H.H. Brongersma, R. ter Veen, J. Huang, H. Guo, Y. Wang, A.K. Datye, Engineering catalyst supports to stabilize PdO_x two-dimensional rafts for water-tolerant methane oxidation, *Nat. Catal.* 4 (2021) 830–839, <https://doi.org/10.1038/s41929-021-00680-4>.
- [34] J. Jones, H. Xiong, A.T. DeLaRiva, E.J. Peterson, H. Pham, S.R. Challa, G. Qi, S. Oh, M.H. Wiebenga, X.L.P. Hernández, Y. Wang, A.K. Datye, Thermally stable single-atom platinum-on-ceria catalysts via atom trapping, *Science* 353 (80) (2016) 150–154, <https://doi.org/10.1126/science.aaf8800>.
- [35] S. Das, A. Jangam, S. Jayaprakash, S. Xi, K. Hidayat, K. Tomishige, S. Kawi, Role of lattice oxygen in methane activation on Ni-phylosilicate@ $\text{Ce}_{1-x}\text{Zr}_x\text{O}_2$ core-shell catalyst for methane dry reforming: Zr doping effect, mechanism, and kinetic study, *Appl. Catal. B Environ.* 290 (2021) 119998, <https://doi.org/10.1016/j.apcatb.2021.119998>.
- [36] D. Guo, M. Li, Y. Lu, Y. Zhao, M. Li, Y. Zhao, S. Wang, X. Ma, Enhanced thermocatalytic stability by coupling nickel step sites with nitrogen heteroatoms for dry reforming of methane, *ACS Catal.* 12 (2022) 316–330, <https://doi.org/10.1021/acscatal.1c04004>.
- [37] K. Bu, S. Kuboon, J. Deng, H. Li, T. Yan, G. Chen, L. Shi, D. Zhang, Methane dry reforming over boron nitride interface-confined and LDHs-derived Ni catalysts, *Appl. Catal. B Environ.* 252 (2019) 86–97, <https://doi.org/10.1016/J.APCATB.2019.04.007>.
- [38] Y. Tang, Y. Wei, Z. Wang, S. Zhang, Y. Li, L. Nguyen, Y. Li, Y. Zhou, W. Shen, F. F. Tao, P. Hu, Synergy of single-atom NiII and RuI sites on CeO_2 for dry reforming of CH_4 , *J. Am. Chem. Soc.* 141 (2019) 7283–7293, https://doi.org/10.1021/JACS.8B10910/ASSET/IMAGES/LARGE/JA-2018-10910A_0010.JPEG.
- [39] M. Akri, S. Zhao, X. Li, K. Zang, A.F. Lee, M.A. Isaacs, W. Xi, Y. Gangarajula, J. Luo, Y. Ren, Y.T. Cui, L. Li, Y. Su, X. Pan, W. Wen, Y. Pan, K. Wilson, L. Li, B. Qiao, H. Ishii, Y.F. Liao, A. Wang, X. Wang, T. Zhang, Atomically dispersed nickel as coke-resistant active sites for methane dry reforming, 2019 101, *Nat. Commun.* 10 (2019) 1–10, <https://doi.org/10.1038/s41467-019-12843-w>.
- [40] K. Cao, M. Gong, J. Yang, J. Cai, S. Chu, Z. Chen, B. Shan, R. Chen, Nickel catalyst with atomically-thin meshed cobalt coating for improved durability in dry reforming of methane, *J. Catal.* 373 (2019) 351–360, <https://doi.org/10.1016/j.jcat.2019.04.017>.
- [41] R. Baran, Y. Millot, T. Onfroy, J.M. Krafft, S. Dzwigaj, Influence of the nitric acid treatment on Al removal, framework composition and acidity of BEA zeolite investigated by XRD, FTIR and NMR, *Microporous Mesoporous Mater.* 163 (2012) 122–130, <https://doi.org/10.1016/j.micromeso.2012.06.055>.
- [42] Y. Wang, Z.P. Hu, W. Tian, L. Gao, Z. Wang, Z.Y. Yuan, Framework-confined Sn in Si-beta stabilizing ultra-small Pt nanoclusters as direct propane dehydrogenation catalysts with high selectivity and stability, *Catal. Sci. Technol.* 9 (2019) 6993–7002, <https://doi.org/10.1039/C9CY01907C>.
- [43] J. Zhang, B. Tang, Z. Zhu, G. Zhao, Size-controlled microporous SiO_2 coated TiO_2 nanotube arrays for preferential photoelectrocatalytic oxidation of highly toxic PAEs, *Appl. Catal. B Environ.* 268 (2020) 118400, <https://doi.org/10.1016/j.apcatb.2019.118400>.
- [44] T.Y. Song, Z.X. Dong, J.D. Song, X.X. Wang, G.Q. Xie, M.F. Luo, J.Q. Lu, Dehydrochlorination of 1, 1, 2-trichloroethane over SiO_2 -supported alkali and transition metal catalysts: tunable selectivity controlled by the acid-base properties of the catalysts, *Appl. Catal. B Environ.* 236 (2018) 368–376, <https://doi.org/10.1016/j.apcatb.2018.04.018>.
- [45] L. Weng, X. Bao, K. Sagoe-Crentsil, Effect of acetylacetone on the preparation of PZT materials in sol-gel processing, *Mater. Sci. Eng. B* 96 (2002) 307–312, [https://doi.org/10.1016/S0921-5107\(02\)00384-7](https://doi.org/10.1016/S0921-5107(02)00384-7).
- [46] O. Daoura, G. Fornasieri, M. Boutros, N. El Hassan, P. Beaunier, C. Thomas, M. Selmane, A. Miche, C. Sasseoye, O. Ersen, W. Baaziz, P. Massiani, A. Bleuzen, F. Launay, One-pot prepared mesoporous silica SBA-15-like monoliths with embedded Ni particles as selective and stable catalysts for methane dry reforming, *Appl. Catal. B Environ.* 280 (2021) 119417, <https://doi.org/10.1016/j.apcatb.2020.119417>.
- [47] K. Wang, Y. Men, S. Liu, J. Wang, Y. Li, Y. Tang, Z. Li, W. An, X. Pan, L. Li, Decoupling the size and support/metal loadings effect of Ni/ SiO_2 catalysts for CO_2 methanation, *Fuel* 304 (2021) 121388, <https://doi.org/10.1016/j.fuel.2021.121388>.
- [48] D. Zhao, X. Tian, D.E. Doronkin, S. Han, V.A. Kondratenko, J.D. Grunwaldt, A. Perechodjuk, T.H. Vuong, J. Rabeah, R. Eckelt, U. Rodemerck, D. Linke, G. Jiang, H. Jiao, E.V. Kondratenko, In situ formation of ZnO_x species for efficient propane dehydrogenation, *Nature* 599 (2021) 234–238, <https://doi.org/10.1038/s41586-021-03923-3>.
- [49] L. Liu, J. Lu, Y. Yang, W. Ruettinger, X. Gao, M. Wang, H. Lou, Z. Wang, Y. Liu, X. Tao, L. Li, Y. Wang, H. Li, H. Zhou, C. Wang, Q. Luo, H. Wu, K. Zhang, J. Ma, X. Cao, L. Wang, F.S. Xiao, Dealuminated beta zeolite reverses Ostwald ripening for durable copper nanoparticle catalysts, *Science* (80) (2023), <https://doi.org/10.1126/SCIENCE.ADJ1962>.
- [50] A. Cárdenas-Arenas, A. Quindimil, A. Davó-Quinonero, E. Bailón-García, D. Lozano-Castelló, U. De-La-Torre, B. Pereda-Ayo, J.A. González-Marcos, J. R. González-Velasco, A. Bueno-López, Isotopic and in situ DRIFTS study of the CO_2 methanation mechanism using Ni/ CeO_2 and Ni/ Al_2O_3 catalysts, *Appl. Catal. B Environ.* 265 (2020) 118538, <https://doi.org/10.1016/j.apcatb.2019.118538>.
- [51] O. Daoura, G. Fornasieri, M. Boutros, N. El Hassan, P. Beaunier, C. Thomas, M. Selmane, A. Miche, C. Sasseoye, O. Ersen, W. Baaziz, P. Massiani, A. Bleuzen, F. Launay, One-pot prepared mesoporous silica SBA-15-like monoliths with embedded Ni particles as selective and stable catalysts for methane dry reforming, *Appl. Catal. B Environ.* 280 (2021) 119417, <https://doi.org/10.1016/j.apcatb.2020.119417>.
- [52] A. Rodríguez-Gómez, R. Pereníguez, A. Caballero, Nickel particles selectively confined in the mesoporous channels of SBA-15 Yielding a very stable catalyst for DRM reaction, *J. Phys. Chem. B* 122 (2018) 500–510, https://doi.org/10.1021/ACS.JPCB.7B03835/ASSET/IMAGES/LARGE/JP-2017-03835H_0014.JPEG.
- [53] C. Rodaun, P. Chaipornchaleram, W. Nunthakitgonson, A. Thivassathit, T. Maihom, T. Atitthep, P. Kidkhunthod, C. Uthayopas, S. Nutanong, S. Thongratkew, K. Faungnawakij, C. Wattanakit, Highly efficient propane dehydrogenation promoted by reverse water–gas shift reaction on Pt–Sn alloy surfaces, *Fuel* 325 (2022) 124833, <https://doi.org/10.1016/j.fuel.2022.124833>.
- [54] M.A. Peck, M.A. Langell, Comparison of nanoscale and bulk NiO structural and environmental characteristics by XRD, XAFS, and XPS, *Chem. Mater.* 24 (2012) 4483–4490, <https://doi.org/10.1021/cm300739y>.
- [55] Z. Bian, N. Dewangan, Z. Wang, S. Pati, S. Xi, A. Borgna, H. Kus, S. Kawi, Mesoporous-silica-stabilized cobalt(II) oxide nanoclusters for propane dehydrogenation, *ACS Appl. Nano Mater.* 4 (2021) 1112–1125, <https://doi.org/10.1021/acsnano.0c02721>.
- [56] Y. Kathiraser, U. Oemar, E.T. Saw, Z. Li, S. Kawi, Kinetic and mechanistic aspects for CO_2 reforming of methane over Ni based catalysts, *Chem. Eng. J.* 278 (2015) 62–78, <https://doi.org/10.1016/j.cej.2014.11.143>.
- [57] D. Shen, Z. Li, J. Shan, G. Yu, X. Wang, Y. Zhang, C. Liu, S. Lyu, J. Li, L. Li, Synergistic Pt– CeO_2 interface boosting low temperature dry reforming of methane, *Appl. Catal. B Environ.* 318 (2022) 121809, <https://doi.org/10.1016/j.apcatb.2022.121809>.
- [58] M. Kosari, S. Askari, A.M. Seayad, S. Xi, S. Kawi, A. Borgna, H.C. Zeng, Strong coke-resistivity of spherical hollow Ni/ SiO_2 catalysts with shell-confined high-content Ni nanoparticles for methane dry reforming with CO_2 , *Appl. Catal. B Environ.* 310 (2022) 121360, <https://doi.org/10.1016/j.apcatb.2022.121360>.
- [59] A.L.A. Marinho, F.S. Toniolo, F.B. Noronha, F. Epron, D. Duprez, N. Bion, Highly active and stable Ni dispersed on mesoporous $\text{CeO}_2\text{-Al}_2\text{O}_3$ catalysts for production of syngas by dry reforming of methane, *Appl. Catal. B Environ.* 281 (2021), <https://doi.org/10.1016/j.apcatb.2020.119459>.
- [60] X. Li, D. Li, H. Tian, L. Zeng, Z.J. Zhao, J. Gong, Dry reforming of methane over Ni/ La_2O_3 nanorod catalysts with stabilized Ni nanoparticles, *Appl. Catal. B Environ.* 202 (2017) 683–694, <https://doi.org/10.1016/j.apcatb.2016.09.071>.
- [61] Q. Zhou, X. Fu, K. Hui Lim, Z. Li, M. Liao, J. Lu, F. Liu, S. Kawi, Complete confinement of Ce/Ni within SiO_2 nanotube with high oxygen vacancy concentration for CO_2 methane reforming, *Fuel* 325 (2022) 124819, <https://doi.org/10.1016/j.fuel.2022.124819>.
- [62] W. Liu, L. Li, S. Lin, Y. Luo, Z. Bao, Y. Mao, K. Li, D. Wu, H. Peng, Confined Ni-In intermetallic alloy nanocatalyst with excellent coking resistance for methane dry reforming, *J. Energy Chem.* 65 (2021) 34–47, <https://doi.org/10.1016/J.JEICHEM.2021.05.017>.